RESEARCH ARTICLE

Key Points:
- Analyzed long-term changes in characteristics of induced seismicity
- Seismicity characteristics reflect fluid migration and increasing pore pressure
- Maximum magnitude related to injection rate and volume of fluids present in reservoir

Correspondence to:
G. Kwiatek,
kwiatek@gfz-potsdam.de

Effects of long-term fluid injection on induced seismicity parameters and maximum magnitude in northwestern part of The Geysers geothermal field

Grzegorz Kwiatek[1], Patricia Martínez-Garzón[1], Georg Dresen[1,2], Marco Bohnhoff[1,3], Hiroki Sone[1,4], and Craig Hartline[5]

[1]Section 3.2: Geomechanics and Rheology, GFZ Potsdam German Research Centre for Geosciences, Potsdam, Germany, [2]Institute of Earth and Environmental Sciences, University of Potsdam, Potsdam, Germany, [3]Institute of Geological Sciences, Free University Berlin, Berlin, Germany, [4]Department of Civil and Environmental Engineering, Geological Engineering Program, University of Wisconsin-Madison, Madison, Wisconsin, USA, [5]Calpine Corporation, Middletown, California, USA

Abstract The long-term temporal and spatial changes in statistical, source, and stress characteristics of one cluster of induced seismicity recorded at The Geysers geothermal field (U.S.) are analyzed in relation to the field operations, fluid migration, and constraints on the maximum likely magnitude. Two injection wells, Prati-9 and Prati-29, located in the northwestern part of the field and their associated seismicity composed of 1776 events recorded throughout a 7 year period were analyzed. The seismicity catalog was relocated, and the source characteristics including focal mechanisms and static source parameters were refined using first-motion polarity, spectral fitting, and mesh spectral ratio analysis techniques. The source characteristics together with statistical parameters (*b* value) and cluster dynamics were used to investigate and understand the details of fluid migration scheme in the vicinity of injection wells. The observed temporal, spatial, and source characteristics were clearly attributed to fluid injection and fluid migration toward greater depths, involving increasing pore pressure in the reservoir. The seasonal changes of injection rates were found to directly impact the shape and spatial extent of the seismic cloud. A tendency of larger seismic events to occur closer to injection wells and a correlation between the spatial extent of the seismic cloud and source sizes of the largest events was observed suggesting geometrical constraints on the maximum likely magnitude and its correlation to the average injection rate and volume of fluids present in the reservoir.

1. Introduction

The need to refine and further develop reservoir engineering techniques such as stimulation of geothermal and (un)conventional hydrocarbon reservoirs, exploitation of deep mines, and underground storage facilities poses fundamental challenges to be addressed such as mitigation of induced seismicity [*Ellsworth*, 2013]. Of special concern in studies of induced seismicity are large magnitude events (LME). LMEs might pose a threat to engineering structures, raise public-acceptance issues, or even cause casualties among underground workers in mines. A striking example is the occurrence of LMEs related to reservoir stimulation within the geothermal Deep Heat Mining project in Basel. A 6 day lasting stimulation of the reservoir for geothermal power production at 5 km depth resulted in occurrence of more than 10,000 seismic events with local magnitudes $M_L > 0.6$ including several magnitude ~3.4 earthquakes [*Deichmann and Giardini*, 2009]. The seismicity was widely felt by the local population raising over \$9M insurance claims and resulting in the shutdown of the project [*Giardini*, 2009]. Recently, the occurrence of LMEs has been reported from hydraulic fracturing operations in south-central Oklahoma [*Holland*, 2013]; waste-water disposal in central Arkansas [*Horton*, 2012]; fluid injection in Youngstown, Ohio [*Kim*, 2013]; induced seismicity during the construction of Gotthard Base Tunnel [*Husen et al.*, 2012]; gas storage [*Cesca et al.*, 2014]; or shale gas fracturing at Blackpool, UK [*Evans et al.*, 2012]. Despite the clear economic and societal relevance of LMEs, a profound understanding of the physical processes leading to their occurrence in response to engineering operations is still lacking.

Mitigation of seismic hazard from induced seismicity is of utmost importance for a safe and efficient (renewable) energy production and development. One of the most debated issues in seismic hazard studies related to induced seismicity is estimating the maximum likely event magnitude [*Convertito et al.*, 2012]. The proposed methods may be divided into deterministic, probabilistic, and empirical [e.g., *Zang et al.*, 2014]. Classical probabilistic seismic hazard assessment procedures require an earthquake catalog and need to account

for specific characteristics of induced seismicity such as nonstationarity or frequently observed non-self-similar behavior of magnitude-frequency distribution [see, e.g., *Lasocki*, 2005; *Lasocki and Orlecka-Sikora*, 2008]. Other methods link the statistical approach with injection procedures and physical properties of the reservoir. For example, *Shapiro et al.* [2007] related the occurrence of maximum magnitude events to the injection duration and to rock properties such as hydraulic diffusivity, and *Shapiro et al.* [2011] to the shortest axis of an ellipsoidal-shaped microseismic cluster. In contrast, *McGarr* [2014] suggested that maximum magnitude is related to the total volume of fluid injected into the reservoir times the shear modulus. *Zang et al.* [2014] reviewed 30 case studies of fluid-induced seismicity (enhanced geothermal system (EGS), geothermal, wastewater disposal, and fracking) and noticed a relation between observed maximum magnitude and injectivity, being the maximum inflow at maximum wellhead pressure. However, the physics governing induced seismicity are still poorly understood and so far few case studies exist that integrate available seismological, geomechanical, and injection/production data.

A comprehensive analysis of induced seismicity requires high-resolution seismicity data. The refinement of hypocenters may be performed using double-difference relocation technique [*Waldhauser and Ellsworth*, 2000], and the spectral parameter quality can be improved by various implementations of the spectral ratio method [*Shearer et al.*, 2006; *Goertz-Allmann et al.*, 2011; *Kwiatek et al.*, 2011, 2014; *Harrington et al.*, 2015]. So far, refinement of source mechanism determination techniques [*Dahm*, 1996; *Andersen*, 2001; *Davi et al.*, 2013] is still rarely applied to induced seismicity data. However, improved focal mechanisms are required to reduce the uncertainty involved in stress tensor inversion [*Michael*, 1987; *Hardebeck and Michael*, 2006; *Martínez-Garzón et al.*, 2014].

The Geysers geothermal field in California represents a unique site for a combined analysis of induced seismicity. The geothermal power production is performed for more than 50 years, and extensive high-quality microseismicity catalog data as well as additional data including geology, stress field, injection, and production data are available. The Geysers is a vapor-dominated reservoir. Over the years, field exploitation resulted in a long-term reduction of reservoir pressure and a decrease in steam production. To recharge the reservoir, fluid injections are performed at The Geysers including two major treated wastewater injection projects Southeast Geysers Effluent Pipeline (since 1997) and Santa Rosa Geysers Recharge Project (SRGRP) (since 2003) [e.g., *Beall and Wright*, 2010]. The SRGRP project resulted in approximately tripling the injection rates in the NW part of the field along with an increased level of induced seismicity throughout the entire field raising concerns of potential environmental and socio-economic impacts on local communities [*Majer and Peterson*, 2007; *Rutqvist and Oldenburg*, 2008]. In addition, the characteristics of seismicity varied between NW and SE parts of the field [*Beall and Wright*, 2010; *Beall et al.*, 2010] in that higher seismic activity and large events with $M > 3.0$ are observed in the NW part of The Geysers [*Sharma et al.*, 2013].

Recently, the immediate response of the reservoir due to fluid injection in the northwestern part of The Geysers (wells Prati-9 and Prati-29) has been studied by *Martínez-Garzón et al.* [2014]. The authors analyzed spatiotemporal changes of the seismicity characteristics including b values, source parameters, and faulting for two fluid injection cycles and suggested that injection of fluids induces thermoelastic and poroelastic stress changes in the reservoir and govern the occurrence of induced seismicity. Changes in the source and statistical parameters of induced seismicity suggested that thermoelastic stress changes dominate close to the well regardless of injection stage, whereas pore pressure diffusion may induce seismicity at larger distances from the well during higher injection rates. This is in agreement with *Rutqvist and Oldenburg* [2008] and *Rutqvist et al.* [2015] who performed coupled thermo-hydrological-mechanical modeling at The Geysers. Their modeling also suggested that thermoelastic cooling near injection wells is the dominant cause of stress changes and resulting seismicity. At greater depths, combined thermoelastic cooling and increased fluid pressure may reduce effective stresses and induce seismicity.

In this study we investigate the long-term (seven years) seismic response of the northwestern part of The Geysers geothermal reservoir to fluid injection. High-resolution source parameters including seismic moment, source radius, static stress drop, and focal mechanisms are combined with statistical catalog parameters (b value) and stress data (stress tensor and stress ratio) to investigate and discuss their long-term temporal and spatial evolution with respect to field operations (injection, production, shut-in, etc.). We present a conceptual model for fluid migration around the two major injection wells of the area that govern induced seismicity recorded during injection. Finally, we discuss potential constraints to maximum magnitude of LME in the investigated area.
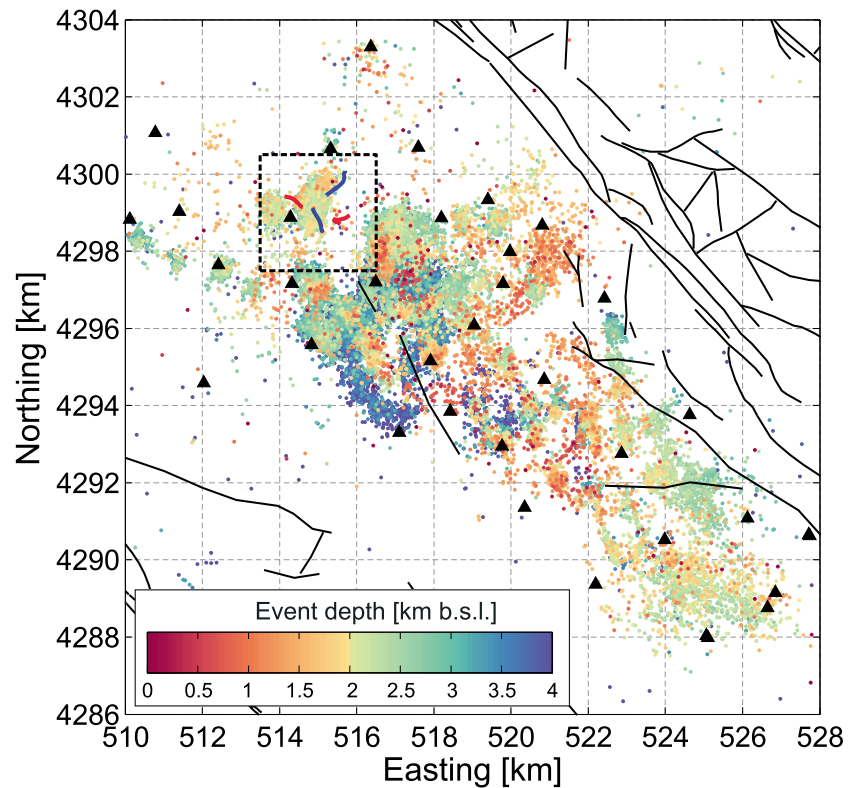
Figure 1. Spatial distribution of seismicity at The Geysers geothermal field ($M_D > 1.0$) for the time period November 2007 to August 2014 with the hypocentral depth being color-coded. The seismic stations are represented by black triangles, and the surface traces of faults are shown as black lines. The study area in the northwestern part of the geothermal field (including well trajectories painted in red and blue) is indicated by the dashed square and enlarged in Figure 2.

2. Data

We investigated seismic data from a distinct cluster of seismicity located in the northwestern part of The Geysers geothermal field (Figures 1 and 2). The selected cluster has a long injection history spanning over 7 years with seasonal injection cycles, abundant seismic activity, and clear temporal correlation between seismicity and injection operations. Injector well Prati-9 operated continuously in the analyzed period between November 2007 and August 2014, and neighboring well Prati-29 operated between April 2010 and June 2013 (Figure 3a). In addition, three production wells are located in the proximity of Prati-9 and Prati-29. Noncondensable-gas concentrations have suggested that the closest production well Prati-25 is not significantly influenced by injections into Prati-9 [*Garcia et al.*, 2012]. For two wells Prati-4 and Prati-5 located east of the analyzed area production started in January 2012. However, as it will be shown later, the production activity in
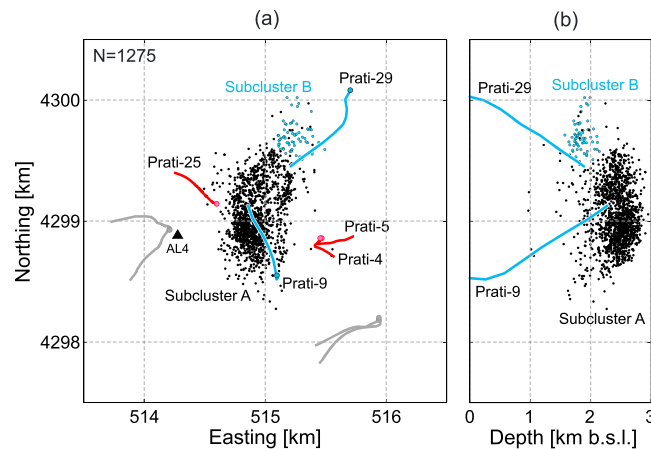
Figure 2. (a) Map view of the relocated seismicity catalogue (1275 events, M_D 1.0–3.2) in the vicinity of the two injection wells Prati-9 and Prati-29. (b) S-N cross section with hypocenter distribution and well trajectories. The events from subclusters A and B are presented using black and blue points, respectively. The injection and production wells are shown as blue and red lines, respectively, and the remaining wells in the vicinity are shown in gray.
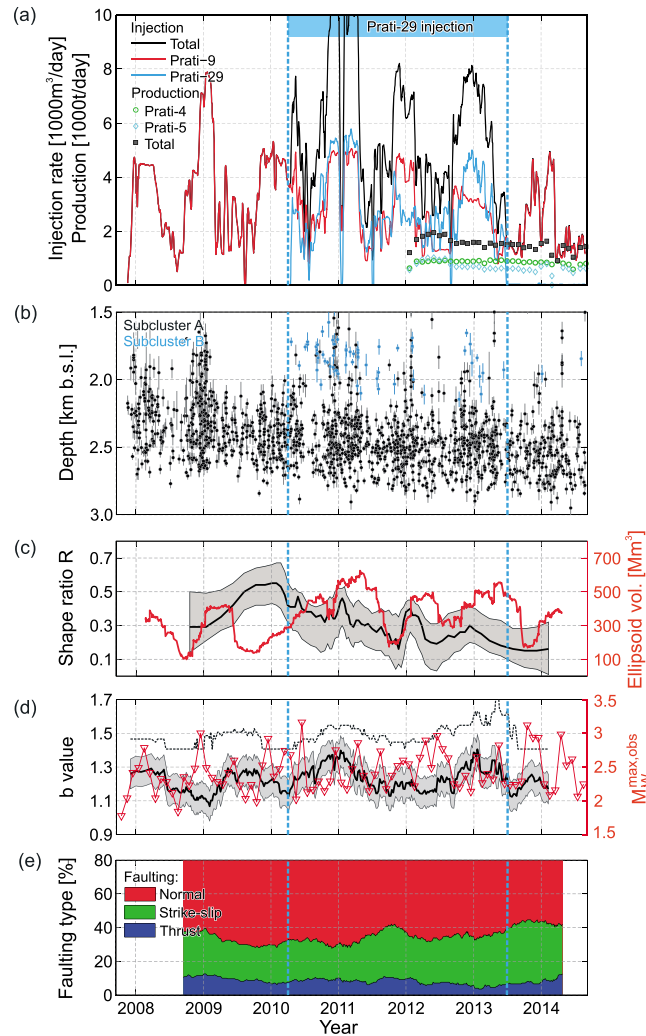
Figure 3. Temporal changes in characteristics of induced seismicity in response to fluid injection into Prati-9 and Prati-29 wells (seismicity catalogue as shown in Figure 2). The injection period into Prati-29 is constrained by dashed blue vertical lines while injection in well Prati-9 was ongoing throughout the entire time interval considered here (7 years). (a) Changes in injection rate into Prati-9 and Prati-29 wells (solid red and blue lines, respectively) and summed total injection rate (solid black line). The production in wells Prati-4 and Prati-5 is shown as green circles and blue rhombs. (b) Changes in hypocenter depths of events with time together with 95% confidence intervals calculated by means of bootstrap resampling. (c) Temporal changes in shape ratio (relative stress magnitude) coefficient (black line with shading denoting 95% confidence interval) and volume of the cluster approximated by ellipsoid using principal component analysis (red line). (d) Temporal changes of the Gutenberg-Richter b value (solid black line with shaded area corresponding to 95% confidence intervals) and magnitude of completeness (dotted line). Red reverted triangles present maximum magnitude observed in each month. (e) Changes in percentage of different faulting types with time.

Prati-4 and Prati-5 has no visible influence on source characteristics of seismicity investigated in this study and it will be ignored.

Between November 2007 and August 2014 about $10.5\,Mm^3$ of treated wastewater was injected into both wells Prati-9 ($7.21\,Mm^3$) and Prati-29 ($3.29\,Mm^3$), with similar average injection rate of $8.79 \times 10^4\,m^3/month$ (Figure 3a). During winter months injection rates were higher than in the summer. The maximum monthly injected volume into Prati-9 and Prati-29 was reached in March 2011 when $3.20 \times 10^5\,m^3$ of water was injected into the reservoir.

The microseismicity was recorded by a local seismic network composed of 31 three-component short-period geophones located on the surface, operated by Lawrence-Berkeley National Laboratory. In addition, larger events are frequently recorded also by distant stations of regional seismic networks. These networks are recording nearly 4000 seismic events per year within The Geysers area with duration magnitude $M_D > 1.0$, which is at the same time approximately the level of completeness of seismic catalog.

The seismicity analyzed in this study is composed of 1776 seismic events recorded over the period of nearly 7 years between November 2007 and August 2014, as reported by Northern California Earthquake data Center (NCEDC). *Martínez-Garzón et al.* [2013, 2014] found a clear relation between seismic activity and injection operations in Prati-9 and Prati-29.

3. Methodology

3.1. Catalog Refinement

The absolute hypocenter and focal mechanism NCEDC catalog contained 1776 events located in the proximity of the Prati-9/Prati-29 system. For 99.8% of events, the duration magnitude M_D was calculated except for the four largest events for which local magnitudes M_L were reported. To unify the magnitudes we assumed $M_L = M_W$ [*Klein*, 2006], and we recalculated M_D to M_W using the formula $M_W = 0.90M_D + 0.47$ [*Edwards and Douglas*, 2014] estimated for The Geysers geothermal field. The magnitude of completeness of the resulting catalog is about $M_W^c = 1.4$ ($M_D^c = 1.0$) and the largest seismic event in the analyzed cluster displayed a

magnitude of $M_W^{\text{max,obs}} = 3.2$. In the original NCEDC catalog the double-couple focal mechanisms are available as they are calculated routinely using FPFIT software [*Reasenberg and Oppenheimer*, 1985] and a 1-D velocity model [*Eberhart-Phillips and Oppenheimer*, 1984].

In a first step the initial hypocenter catalog was substantially refined. We first applied the double-difference relocation technique [*Waldhauser and Ellsworth*, 2000] to improve the internal precision of hypocenter locations. The relocation uncertainties were calculated following the bootstrap approach [*Waldhauser and Ellsworth*, 2000]. The application of the double-difference technique allowed improving the internal precision of hypocenter location relocations down to approximately 50 m. This allowed us to distinguish two major spatial subclusters of analyzed seismicity and resolved long-term temporal changes in hypocentral depth discussed in the following sections.

After relocation of earthquakes focal mechanisms were recalculated with the software HASH [*Hardebeck and Shearer*, 2002], using most of the available first motion polarities with quality weights 0 (best quality) or 1. An average of 26 first-motion polarities per event are used to determine focal mechanisms. The corresponding new takeoff angles were estimated using the 1-D velocity model from *Eberhart-Phillips and Oppenheimer* [1984]. From all acceptable fault plane solutions fitting the polarities, only one (preferred) solution was used here. Finally, the relative orientations of *P*, *T*, and *B* axes with respect to the vertical direction were used to categorize the investigated earthquakes into normal, strike-slip, and thrust events. The final relocated catalog with refined source focal mechanisms contained 1275 events.

3.2. Long-Term Temporal Characteristics

The long-term temporal variations of the relocated seismicity catalog were investigated. The catalog was split into a number of overlapping time windows. For each window, various cluster and seismic source characteristics were calculated. The time-dependent changes in Gutenberg-Richter *b* value together with magnitude of completeness were estimated in a moving time window composed of 200 events using the goodness of fit method [*Wiemer and Wyss*, 2000], assuming that 95% of the catalog can be explained by the Gutenberg-Richter distribution. A window size of 150 days was used to investigate temporal changes in the spatial characteristics of the relocated seismicity. For each time window we calculated the best fitting ellipsoid to the spatial distribution of relocated earthquake hypocenters using principal component analysis, assuming that approximately 95% of all events are located inside the ellipsoid. The resulting time-dependent matrix representation of the ellipsoid was used to extract the temporal changes in ellipsoid semiaxis directions and lengths. Time-dependent changes of the hypocentral distribution are given by the volume of the ellipsoid and three semiaxis lengths. The relative contribution of different faulting regimes (normal, strike-slip, and thrust faulting) was calculated in moving time windows of 150 events. We used the MSATSI software [*Martínez-Garzón et al.*, 2014] based on the SATSI package [*Hardebeck and Michael*, 2006] to invert the focal mechanisms for the stress tensor orientation and the stress shape ratio $R = (\sigma_1 - \sigma_2)/(\sigma_1 - \sigma_3)$ in moving time windows of 55 events and an overlap of 10 events. Here uncertainties were estimated by performing 2000 bootstrap resampling of the original data set by selecting randomly one of the two possible fault planes.

3.3. Source Parameters

The source parameters assessment is composed of two steps. First, the initial estimation of source parameters is performed using the spectral fitting method. In the following, the source parameters are refined by application of the mesh spectral ratio technique that is applied to the whole cluster of seismicity. We used the stations from Berkeley-Geysers (BG) network only, as this network provide a consistent instrumentation, high sampling rate, and good signal-to-noise ratio for the whole analyzed catalog, which was required in the course of processing.

The three-component waveforms from stations with a significant signal-to-noise ratio of 20 dB were filtered using a 1 Hz high-pass Butterworth filter. *P* and *S* waveforms were analyzed with a window length of 0.40 s with additional 0.10 s period prior to either *P* or *S* wave onsets, respectively. The windows were smoothed using von Hann's taper, and the far-field ground velocity spectra were estimated from all three components using the multitaper method [*Percival and Walden*, 1993] and then combined altogether [e.g., *Abercrombie*, 1995]. The observed ground velocity spectra were fit to Boatwright's point-source model [*Boatwright*, 1978]:

$$\dot{u}^{\text{th}}(f; M_0, f_C, Q_C) = \frac{R_C}{2\rho V_C^3 R} \frac{fM_0}{\left(1 + (f/f_C)^4\right)^{0.5}} \exp\left(-\frac{\pi R f}{Q_C V_C}\right), \tag{1}$$

where R is the source-receiver distance, M_0 is the seismic moment, f_C is the corner frequency, Q_C is the quality factor, and R_C is the average radiation pattern correction coefficient of either P or S waves. Following *Boatwright and Boore* [1982], we applied $R_P = 0.52$ and $R_S = 0.63$ for P and S waves, respectively. We assumed $V_P = 4785$ m/s and $V_S = 2848$ m/s, the averaged P or S wave velocity in the source area, assuming $V_P/V_S = 1.68$ [*Gritto and Jarpe*, 2014] and a density of $\rho = 2700$ kg/m. We invert for $[M_0, f_C, Q_C]$ by optimizing the cost function $\left\| \log(\dot{u}^{\text{th}}(f; M_0, f_C, Q_C)) - \log(\dot{u}(f)) \right\|_{L1} = \min$, where $\dot{u}(f)$ is the observed ground velocity amplitude spectrum for a particular station and phase. The optimization was performed by means of grid search and simplex techniques [cf. *Kwiatek et al.*, 2011, 2014], resulting in 882 events with successfully recalculated seismic source parameters.

3.3.1. Spectral Ratio Refinement

To further improve static source parameters $[M_0, f_0]$ and reduce the attenuation effects we applied the mesh spectral ratio technique [*Kwiatek et al.*, 2011, 2014; *Harrington et al.*, 2015]. The spectral ratio technique suppresses poorly resolved travel path effects, site response, and the instrument response so that spectral corner frequency and seismic moment are more accurately estimated from the earthquake source spectrum.

In the first step we measured the similarity between 882 events with source parameters calculated using the spectral fitting method. We define a distance metric that combines Cartesian distance between two events i and j forming the cluster, moment magnitude difference between events and focal mechanism similarity measured as minimum 3-D rotation angle required to overlap P, T, and B axes of the two focal mechanisms forming a pair [*Kagan*, 1991, 2007]. The shortest "distances" were obtained for *co-located events* displaying *similar focal mechanism* and *significant differences in calculated magnitudes*. Larger distances were obtained for pairs of events located far away from one another and/or with different focal mechanisms and/or with similar magnitudes. This approach allowed us to categorize pairs of events on the basis of how well they fulfill the criteria for deconvolution of propagation effects using empirical Green's function [*Hartzell*, 1978; *Mueller*, 1985; *Kwiatek*, 2008] (see Text S1 in the supporting information for details). The removal of propagation effects by empirical Green's function (eGf) deconvolution method requires a pair of co-located events with similar focal mechanism and sufficient magnitude difference ($\Delta M > 1.0$), i.e., the event pairs with small distances in a defined distance metric.

For each event i and j we computed a ratio of ground velocity spectra at station k:

$$\Psi^{ij}\left(f; M_0^i, M_0^j, f_0^i, f_0^j\right) = \frac{\dot{u}\left(f; M_0^i, f_0^i\right)}{\dot{u}\left(f; M_0^j, f_0^j\right)} = \frac{M_0^i}{M_0^j} \left(\frac{1 + \left(\frac{f}{f_0^j}\right)^4}{1 + \left(\frac{f}{f_0^i}\right)^4} \right)^{0.5}. \tag{2}$$

The ratio in equation (2) is generated only if the "distance" between i and j is sufficiently small; i.e., only pairs of events fitting the eGf criteria are linked (see Text S1 for details). Ratios are formed for the whole cluster generating a mesh of Ψ^{ij}. For earthquakes with small distances to numerous neighboring events numerous ratios Ψ^{ij} exist. From equation (2) it is clear that the propagation, site, and sensor effects are largely removed. Also, the static source parameters $[M_0, f_0]$ of a particular event are depending on source parameters of other (likely numerous) neighboring events. To improve the quality of corner frequency and seismic moment estimates many spectral ratios are combined to constrain the source parameters of a single event. The nonlinear inverse problem consists in finding an optimum configuration of source parameters for all events $M_0 = \left[M_0^1, M_0^2, \ldots, M_0^N\right]$ and $f_0 = \left[f_0^1, f_0^2, \ldots, f_0^N\right]$ forming a cluster that minimizes the following cost function [cf. *Kwiatek et al.*, 2014]:

$$\epsilon(M_0, f_0) = \sum_k \sum_{i,j} w_{ij} \left\| \log \Psi^{ij}(f) - \log \Psi^{ij}_{\text{observed}}(f) \right\|_{L1} = \min, \tag{3}$$

where summation accounts for all pairs (i, j) of spectral ratios formed at station k and w_{ij} is a weighting factor related to distance' between event i and j. Instead of optimizing the equation (3), we sampled the *a posteriori* distribution $\exp(-\epsilon(M_0, f_0)/T)$ using Monte Carlo-based Metropolis Hastings Random Walk [*Metropolis et al.*, 1953; *Hastings*, 1970; *Mosegaard and Tarantola*, 1995]. The constant T determined the model acceptance rate for cases where the error function of the new model exceeds the error function of the previous model. We determine our T value by trial and error to correspond to a 50% acceptance rate. The obtained *a posteriori* distribution pdf(M_0, f_0) was used to calculate 2-D marginal probability density distributions pdf
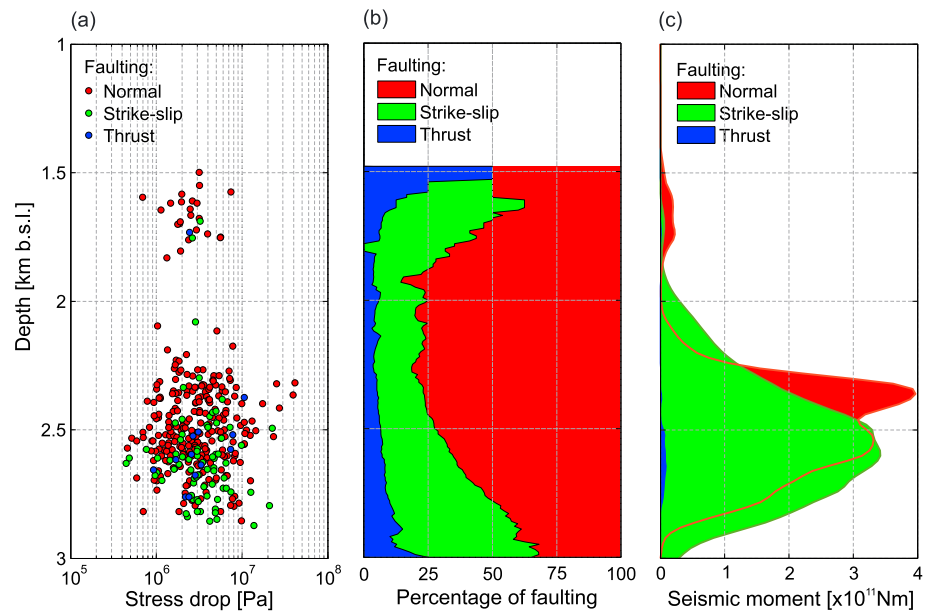
Figure 4. (a) Changes in static stress drop; (b) proportion between percentage of strike-slip, normal, and thrust faulting events; and (c) seismic moment release with depth. The static stress drop values were refined by means of mesh spectral ratio technique (see text for details). The proportions of different faulting types are calculated on the basis of accepted focal mechanisms derived from the HASH software.

$\left(M_0^i, f_0^i\right)$ for each event refined with spectral ratio technique. Seismic moments (M_0) and corner frequencies (f_0) were calculated as average model from marginal distributions. If the marginal 2-D distribution from a particular event displayed a non-Gaussian shape, the event was rejected. Using this approach we obtained 354 events with refined source characteristics.

The source radius r_0 was calculated from corner frequencies estimated using the spectral ratio technique and assuming the circular source model of *Madariaga* [1976] with scaling constant $k = 2.01$ corresponding to constant rupture velocity of $0.9V_S$. The moment magnitudes were calculated using the formula of *Hanks and Kanamori* [1979]: $M_W = 0.66 \log_{10} M_0 - 6.03$. Finally, static stress drops were calculated from M_0 and r_0 following *Eshelby* [1957], $\Delta\sigma = \frac{7}{16}\frac{M_0}{r_0^3}$.

4. Results

4.1. Lateral and Depth Changes of Seismicity

Figure 2 displays the epicenter distribution and S-N section of the relocated seismicity derived in this study. Two distinct spatial subclusters of seismicity can be identified. Subcluster A contains the majority of observed events close to well Prati-9 with seismic activity lasting from November 2007 until August 2014. In general, the seismicity from subcluster A is deeper (up to 300 m) than the open-hole section of well Prati-9. Most events occur below 2 km depth between the normal temperature reservoir (NTR) and the transition into the high temperature zone (HTZ) below [*Garcia et al.*, 2012; *Jeanne et al.*, 2014]. At this depth interval the formation temperature changes drastically from 200°C to 400°C. Seismicity of subcluster B started to become active with the onset of injection into Prati-29 in April 2010 and slowly ceased after the shut-in of the well in summer 2013. Hypocentral depths of the observed seismicity correspond to the injection interval of Prati-29 (NTR).

Seismic moment release, static stress drop, and the distribution of fault types as a function of event depths are presented in Figure 4. For the seismic moment release changes with depth (Figure 4c), the curves were calculated using a sum of Gaussian functions with amplitude corresponding to seismic moment and standard deviation reflecting the source radius of investigated events. Most of the seismic moment is released in the central part of the reservoir at a depth between 2.3 and 2.7 km by normal or strike-slip events. The maximum seismic moment release from strike-slip events occurs slightly deeper by about 300 m compared to the
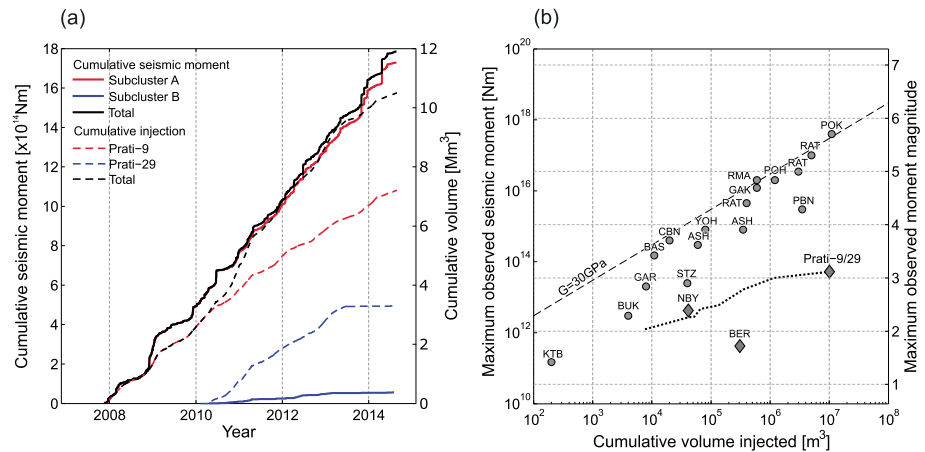
Figure 5. (a) Temporal evolution of cumulative seismic moment released in subclusters A and B plotted as solid red and blue lines, respectively. The corresponding cumulative fluid injection in Prati-9 and Prati-29 wells is presented as dashed red and blue lines. The total seismic moment release and total cumulative injection from both wells are shown with solid and dashed black lines. (b) Relation between cumulative volume of fluid injected and maximum observed seismic moment for a number of sites including wastewater disposal, geothermal, fracking, and scientific projects (gray circles, adapted from *McGarr* [2014]). The additional hydrothermal sites (rhombs) include this study as well as data from Newberry volcano project [*Osborn et al.*, 2011; *Cladouhos et al.*, 2013] and Berlín Geothermal Field [*Kwiatek et al.*, 2014]. The evolution of the maximum observed magnitude with cumulative injection rate for Prati-9 and Prati-29 is shown by the dotted thick line. The theoretical limit to maximum magnitude assuming shear modulus of 30 GPa is indicated by the dashed line.

maximum seismic moment release from normal faulting events. Also, the contribution of strike-slip and thrust events increase with depth at the expense of normal faulting events (Figure 4b). Low static stress drop values are predominantly observed for normal faulting events as opposed to strike-slip faulting events that have slightly higher static stress drops (Figure 4a). The increased number of strike-slip events at greater depths with slightly higher stress drops may be related to an increase in horizontal and mean stress.

### 4.2. Long-Term Temporal Changes of Seismicity

The long-term temporal changes in seismicity during injection operations performed at wells Prati-9 and Prati-29 generally exhibit an increase in event depth within subcluster A (Figure 3b). The deepening of seismicity starts with injection operations at well Prati-9, continues during concurrent Prati-9 and Prati-29 injections and becomes less pronounced starting 2012 or even stopped after shut-in of Prati-29 injection in June 2013. In contrast, seismicity of the shallower subcluster B close to well Prati-29 shows no deepening with time.

The volume of subcluster A changes in response to injection into Prati-9 and Prati-29 reaching a maximum of 600 Mm^3 when both wells are operating. The shut-in of Prati-29 resulted in a decrease in cluster volume back to values observed before combined injection. This indicates that injection from Prati-29 contributes also to the spatial changes of seismicity in the larger subcluster A.

The stress shape ratio $R = (\sigma_1 - \sigma_2)/(\sigma_1 - \sigma_3)$ shows seasonal changes and a general decrease after 2010 (Figure 3c). It first increased up to $R = 0.6$ at the beginning of 2010. Once injection in well Prati-29 started, the parameter shows an overall decrease.

At reservoir depth the dominating mechanism is normal faulting (60% of all events) (Figure 3e) [see also *Martínez-Garzón et al.*, 2013]. Strike-slip focal mechanisms, located slightly deeper in the reservoir (cf. Figure 4b), contribute by about 30%, and the remaining ~10% display thrust faulting. A slight but persistent increase in the relative amount of strike-slip events with time is observed in response to injection into Prati-29 at the cost of reduction in relative amount of normal faulting events.

Figure 3d presents temporal changes in the Gutenberg-Richter b value calculated using the goodness of fit method allowing for a variable M_W^C (estimated for each time window concurrently with a b value). We also tested the b value changes assuming that constant magnitude of completeness is equal to $M_W^C = 1.4$, and different moving windows of different sizes finding the reasonable choice of above parameters do not affect the estimation of b value significantly. The short-term temporal changes in b value are visible; however, no
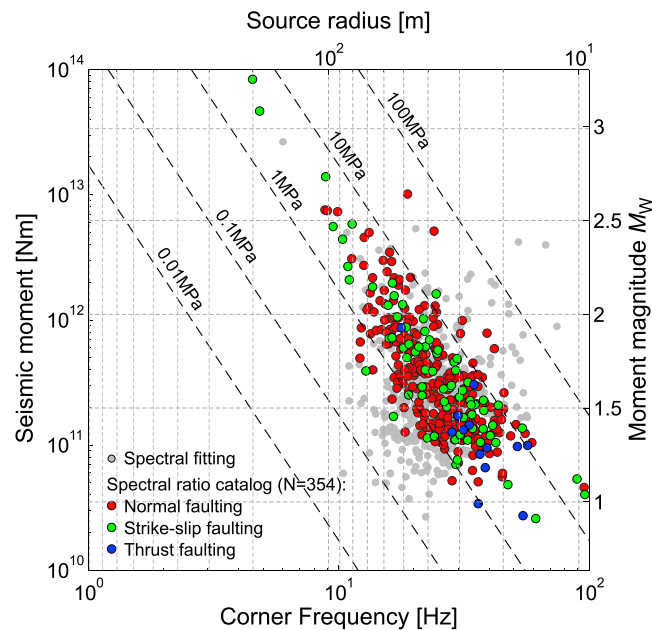
Figure 6. The dependence between corner frequency (source radius, estimated assuming Madariaga source model) and seismic moment (moment magnitude) for the data set refined with the mesh spectral ratio technique (see text for details). The results are color-coded with focal mechanism type. The initial source parameters estimated using spectral fitting method are shown for comparison using gray circles.

long-term trend is observable. The average b value is $\bar{b} = 1.22 \pm 0.08$ throughout the whole observation period. This value is comparable with that reported field-wide ($b = 1.2$) at The Geysers [*Dempsey and Suckale*, 2015], $b = 1.28 \pm 0.03$ reported by *Convertito et al.* [2012] as well as with the results of laboratory experiments on rock samples taken from the three well bores at The Geysers geothermal field where a $b = 1.3$ was observed [*Lockner et al.*, 1982].

4.3. Cumulative Seismic Moment Release and Maximum Likely Magnitude

Long-term cumulative seismic moment release in the vicinity of the investigated cluster increases almost linearly (Figure 5a) and is only slightly affected by the start of injection at Prati-29. The cumulative seismic moment release in subcluster A contributes the vast majority (~97%) to the total cumulative seismic moment observed; subcluster B located in the

vicinity of Prati-29 contributes only a very minor portion (~3%). Despite the fact that injection well Prati-29 roughly doubled the injection rates in the area, the cumulative seismic moment release in the vicinity of Prati-29 (subcluster B) is approximately 30 times lower than that observed in subcluster A, accompanied by the low seismic activity in the vicinity of Prati-29 well. Neither cumulative seismic moment release nor seismic activity did increase significantly in subcluster A due to the doubled injection rates.

Figure 5b presents the dependence between the total cumulative volume injected into the reservoir and the maximum moment magnitude observed therein. *McGarr* [2014] first suggested an upper bound for M_0^{max}, $M_0^{max} = G\Delta V$, where G is the shear modulus and ΔV is the change in the volume injected. The combined injection into the Prati-9 and Prati-29 system until August 2014 amounts to a total injected volume of 10.5 Mm^3. For this time period the maximum observed magnitude in our data set is $M_W^{max,obs} = 3.2$, corresponding to the maximum observed seismic moment of 6.1×10^{13} Nm. This is significantly lower than expected from $M_0^{max} = G\Delta V$ relation, which would predict a maximum magnitude of M_W 5.5 corresponding to the seismic moment of 2.3×10^{17} Nm for the comparable volume of fluids injected. The maximum observed magnitude is also lower than that observed in massive wastewater injections.
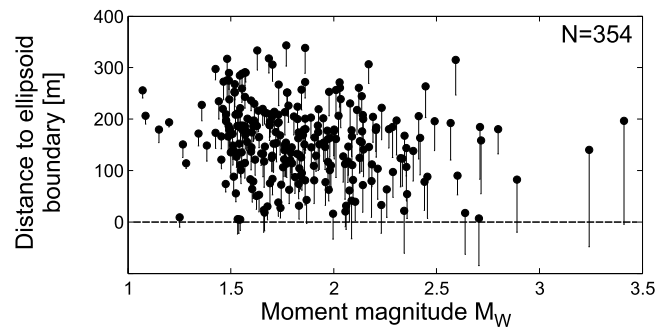
4.4. Source Parameters

The spectral fitting method resulted in estimations of corner frequency, seismic moment, radiated energy, and attenuation (the latter for P and S waves). We found very good agreement between seismic moments estimated exclusively from P and S wave phases with the relation $M_W^s = 1.03 M_W^p + 0.02$. Also, the relation between duration magnitude M_D and moment magnitude M_W for the analyzed cluster using S wave data, $M_W = 0.88 M_D + 0.55$, was found to be very similar to that reported by other authors for the whole field [*Sharma et al.*, 2013; *Edwards and Douglas*, 2014].

The catalog of 354 events refined by means of spectral ratio method indicates constant static stress drop scaling with now reduced scatter in observed static stress drop values not exceeding 1.5 order of magnitude (Figure 6) [cf. *Kwiatek et al.*, 2011]. The average value of static stress drop of about 7 MPa is observed assuming the Madariaga source model. This value is somehow lower than that observed by *Viegas and Hutchings* [2011]

Figure 7. The dependence between moment magnitude of an earthquake and its distance to the cluster boundary approximated by ellipsoid calculated at the moment of earthquake occurrence. The source radius estimated from corner frequency assuming Madariaga source model is shown with a line pointing downwards. The catalog refined with mesh spectral ratio technique ($N = 354$ events) for which high-quality source radii were calculated was used.

who used the empirical Green's function technique and NetMoment methods to investigate the source properties of seismicity in the same Prati-9 system and obtained the median stress drop of 28 MPa. In contrast, *Convertito et al.* [2015] reported low stress drop values of 2 MPa at The Geysers using the iterative multistep inversion of source parameters [*Zollo et al.*, 2014]. The seismicity refined with the spectral ratio technique is self-similar and does not display any signatures of scaling breakdown, which was visible in the source parameters calculated using the spectral fitting method only (gray points in Figure 6). Finally, the LME moment magnitude estimated by spectral ratio technique was slightly higher than that from original catalog and equaled $M_W^{max,obs} = 3.4$.

We tested whether static stress drops display a distance-dependence with respect to the well or a depth-dependence. The distance-dependence of stress drop was previously reported in studies of fluid-induced seismicity at Basel, Switzerland, and at Berlín Geothermal Field, El Salvador [*Goertz-Allmann et al.*, 2011; *Kwiatek et al.*, 2014], and attributed to the expansion of the pore pressure front and increase in pore pressure due to injection. For the data analyzed here we do not observe any significant dependence of static stress drop on distance from the injection site. Similarly, no changes of static stress drop with time have been found.

Finally, we analyzed the location of seismic events with respect to the temporal variations of the volume of the seismic cloud (Figure 7). Interestingly, larger events with $M_W > 2.5$ and their fault planes are contained inside the cluster. This is in contrast to other studies, where LMEs are reported to occur at the margin of the seismic cloud [*Baisch et al.*, 2006; *Majer et al.*, 2007; *Bachmann et al.*, 2012].

5. Discussion

Stark [1992] suggested that microseismicity induced at The Geysers is caused by liquid water injected into the reservoir based on isotopic data. Recent studies of *Martínez-Garzón et al.* [2014] and *Jeanne et al.* [2014] also emphasized that fluid injection at The Geysers caused the observed seismicity due to induced thermal and/or poroelastic stress changes in the reservoir. Therefore, understanding fluid migration and pore pressure changes with respect to injection operations and the influence of different mechanisms inducing the seismicity are important factors to assess the expected seismic response of the reservoir. Here we first present a conceptual model of fluid transport in the vicinity of Prati-9 and Prati-29 interpreted from the analysis of induced seismicity and available technological information. Subsequently, we discuss potential limits on the maximum magnitude to be expected in response to the injection in the study area.

5.1. Seismic Response Versus Long-Term Fluid Injection and Production

The observed long-term temporal variations in seismicity and local stresses are strongly correlated to changes in injection operations performed at both wells. In 2012, the production started in Prati-4 and Prati-5 wells located in proximity of investigated area. The two production wells show approximately constant production level without seasonal changes (the combined monthly production rate is never larger than combined injection rate into Prati-9 and Prati-29 wells). This is different from the observations at field scale, where the global production at The Geysers correlates with injection operations. The two production wells located close to analyzed injectors show slowly decreasing wellhead temperatures which did not exceed several degree Celsius, in agreement with what was observed in other areas of The Geysers geothermal field [*Goyal*, 1998]. Also, an increase in temperature after shut-in of Prati-29 by approximately 30°C was observed. However, the characteristics of seismic parameters remain fully unaffected by introduction and

continuation of production operations, suggesting that seismicity observed in Prati-9/Prati-29 is correlated to fluid injection rather than to fluid production.

Short-term seasonal changes in the volume of the seismic cloud were attributed to changing fluid injection rates and pore pressure perturbations [*Martínez-Garzón et al.*, 2014]. The authors found that during periods of high injection rates, the seismic cloud expanded predominantly along the direction of maximum horizontal stress. Here we tried to suppress the short-term changes by incorporating a wider time windows and investigate the long-term lateral cluster changes. Nevertheless, short-term high-frequency temporal changes in cluster size are still visible.

The migration of fluids toward deeper parts of the reservoir is documented by changes in hypocentral depths of relocated seismicity (Figure 3b). Such migration is expected, as the subhydrostatic reservoir pressures observed at The Geysers cause the injected water to flow downward, which is additionally facilitated by steeply dipping fault planes [*Boyle and Zoback*, 2014]. Depth migration begins already with the injection into Prati-9; however, it is most intense during combined injection into both wells resulting in doubled injection rates. Finally, the depth migration seems to decelerate after the shut-in of Prati-29. It is therefore conceivable that the additional factor accelerating the depth migration is an increasing volume (approximate weight) of water in the reservoir itself due to the doubled injection rates. These fluids increase the pore pressure at greater depths, especially during periods of high injection rates, resulting in peculiar characteristics of induced seismicity observed therein suggesting the operation of poroelastic stresses and existence of water in liquid state (Figure 4). Moreover, the increased injection rates (seasonal or due to combined injection into both wells) cause a proportional increase in the volume of fluids in the reservoir, which is observed by temporal expansion of the seismic cloud (Figure 3). The excess of water in the reservoir at high injection rates leads to boiling suppression due to increased hydrostatic pressure [*Stark*, 2003; *Beall et al.*, 2010], which is apparent during combined injection in Prati-9 and Prati-29 as expansion of the seismic cloud. The observed increase in the relative amount of events displaying strike-slip focal mechanisms at greater depths (Figure 4b) may be explained by increased fluid pressure due to the injection of fluids into the reservoir assuming penny-shaped reservoir model [*Segall and Fitzgerald*, 1998]. It is also worth to note that the largest increase of strike-slip faulting events is occurring during the combined injection into Prati-9 and Prati-29, where the fluid pressure at the bottom of the reservoir is expected to be the highest.

We have observed a long-term temporal decrease in the stress shape ratio R. The observed stress regime is normal faulting, and thus, assuming that the absolute vertical stress $S_V = S_1$ remains approximately constant with pore pressure variations and that the pore pressure tends to increase in the long-term, the observed reduction in the shape ratios with time may be explained by the combination of a decrease in all effective stresses due to pore pressure increase as well as an increase of absolute horizontal stresses due to poroelastic effects [*Schoenball et al.*, 2010; *Altmann et al.*, 2014]. This links the decrease in stress shape ratio to relative positive change in S_2 with respect to S_3 at constant S_1. Interestingly, an increase of the intermediate stress also stabilizes the elastic behavior of rocks [*Takahashi and Koide*, 1989; *Fjær and Ruistuen*, 2002] shifting failure to higher stress levels.

The total seismic moment released in subcluster B during the injection in both wells at similar rates is 30 times lower than observed for the deeper subcluster A during injection in Prati-9 only. Therefore, one might expect that water injected into Prati-29 caused only a limited amount of seismicity at shallower depths, but migrated downward contributing to the seismicity and seismic moment release in subcluster A. There, we do observe changes in spatial and physical properties of the seismicity. However, we do not observe any visible accelerating seismic moment release due to the combined injection in both wells. This particular behavior could be partially explained using a conceptual model of seismicity triggering mechanism for HTZ (high temperature zone) and NTR (normal temperature reservoir) zones at The Geysers [*Stark*, 2003]. The water with a temperature of approximately 70℃ is injected through Prati-29 well into the NTR zone (Figure 8). It heats to the NTR reservoir temperature of about 240℃ generating seismicity induced by thermal stress changes and continues depth migration through the NTR zone. The heated water reaches HTZ reservoir at greater depth, where it is affecting the properties of induced seismicity due to the increased pore fluid pressure at greater depths, but not contributing significantly to the seismic moment release due to the relatively low temperature contrast between water and rocks. On the other hand, the water injected into Prati-9 reaches directly the HTZ boundary resulting in large thermal contrast between rocks and injected water. This suggests more pronounced
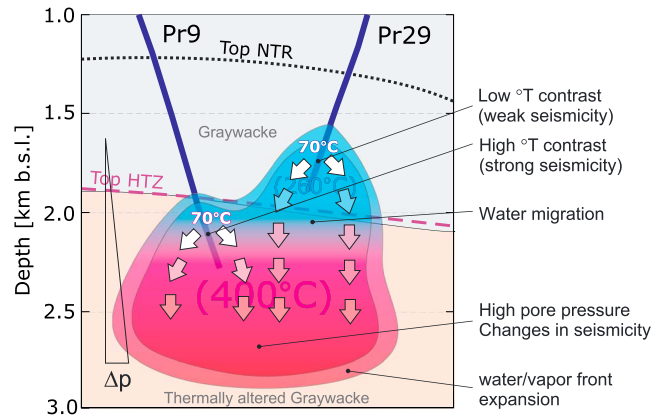
Figure 8. The conceptual model of fluid propagation in the vicinity of Prati-9 and Prati-29 wells (see manuscript for details).

seismicity with generally large seismic moment release due to operations performed in Prati-9 in subcluster A in comparison to that from Prati-29 in the subcluster B. Therefore, it seems that the thermal stresses are responsible for the long-term seismic moment release and seismic activity, whereas poroelastic stresses seem to affect the characteristics of seismicity at greater depths, (i.e., higher pore fluid pressure), as well as at greater distances from the well.

The introduction of Prati-29 injection essentially doubled injection rates and increased the volume of water in the reservoir. The long-term tendency presents a positive change in the subcluster A volume by approximately a factor of 1.5 after injection in Prati-29 started. Note that the volume of subcluster A decreased after shut-in of the well Prati-29. This indicates the influence of injection at well Prati-29 on evolution of subcluster A.

In summary, the spatial and the long-term temporal behavior of the seismicity cloud, as well as the induced seismicity characteristics, suggest the elastic response of the reservoir to the injection operations performed in both Prati-9 and Prati-29 wells. Both thermoelastic and poroelastic effects operate concurrently with thermoelastic effects dominating the seismic activity and moment release provided that significant thermal stresses are present. The influence of poroelastic effects on seismic moment release is unclear; however, on long term they do seem to affect the source characteristics of seismicity, especially in the deeper part of the reservoir where poroelastic stresses are larger. The observed microearthquakes are related (but not necessarily limited) to the plume of water that changes its volume due to short-term and long-term changes in the injection rate. The short-term changes are related to seasonal changes in the amount of water injected [*Stark*, 2003; *Beall et al.*, 2010; *Martínez-Garzón et al.*, 2014], and the long term changes are related to the introduction and shut in of well Prati-29.

5.2. Upper Limit to the Maximum Expected Magnitude

McGarr [2014] derived an empirical relation estimating the maximum expected magnitude of seismic events from the total amount of fluid injected in a reservoir:

$$M_0^{max,McGarr} = \frac{1-B}{B} \frac{2\mu(3\lambda + 2G)}{3} \Delta V, \qquad (4)$$

where $B = b/1.5$, μ is the friction coefficient, and λ and G are Lame's elastic parameters with G being the modulus of rigidity. Assuming $b = 1$ and $\lambda = G$, and a coefficient of friction of $\mu = 0.6$, we obtain a simplified relation (dashed line in Figure 5b):

$$M_0^{max,McGarr} = G\Delta V. \qquad (5)$$

However, the observed maximum expected magnitude ($M_W^{max,obs} = 3.2$ from catalog data) for the studied part of The Geysers is significantly lower than predicted from equation (4). Assuming observed $b = 1.22$, shear modulus of $G = 22$ GPa, and a friction coefficient of $\mu = 0.68$ [*Lockner et al.*, 1982] and Lame's constant $\lambda = 18$ GPa calculated from V_P/V_S ratio [*Gritto and Jarpe*, 2014], the predicted maximum moment from equation (4) is $M_W^{max,McGarr} = 5.0$ for a fluid injection of 3.41 Mm^3 until the occurrence of LME. This value is even larger than the maximum magnitude observed at The Geysers field-wide until today (M_W 4.68).

5.2.1. Maximum Magnitude and the Thickness of the Reservoir

The first considered upper limit to the maximum magnitude observed in the analyzed seismicity cloud could be related to the geometrical constraints of the reservoir. This type of upper constraint to the magnitude has been reported recently [e.g., *Eaton et al.*, 2014]. In our case, the thickness of the seismically active part of the
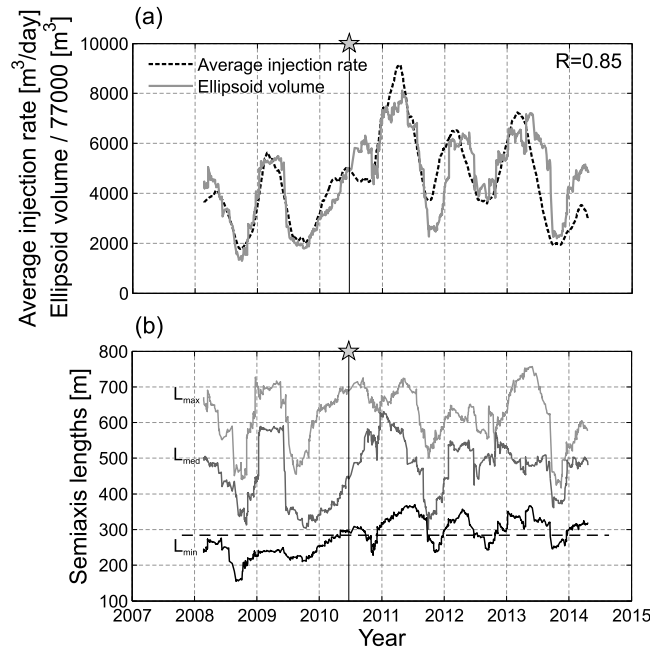
Figure 9. (a) Temporal changes in average injection rate (dashed black line) and cluster volume approximated by ellipsoid (solid gray line) calculated in a moving time window of 150 days. The occurrence of the largest event is marked with yellow star. High correlation between this these two quantities is visible. (b) Temporal changes in semiaxis lengths of the ellipsoid calculated from relocated hypocenters by means of principal component analysis (see text for details). The average value of shortest semiaxis length is shown with dashed black line (note that the shortest semiaxis length does not change significantly with time).

reservoir in the area of Prati-9 and Prati-29 deduced from the vertical span of the relocated seismicity (cf. Figure 3) can be approximated as 1 km. In addition, the largest lateral extension of subcluster A at the time of peak injections into Prati-9 and Prati-29 does not exceed about 1 km × 2 km. Assuming the average stress drop to be on the order of about 7 MPa, as estimated using the spectral ratio technique (Figure 6), and assuming that the potential earthquake LME will rupture through the entire seismicity cloud with a rupture surface of approximately $8.14 \times 10^5 \, m^2$ (i.e., that the potential fault plane will not exceed the size of the cluster at its peak which was noted in December 2012) this will result in a maximum expected magnitude in the vicinity of Prati-9/Prati-29 system of M_W 4.2. We cannot rule out that the rupture extended beyond the cluster boundaries. However, our observations suggest that the fault planes of the larger events are rather confined to cluster boundaries (cf. Figure 7). Interestingly, the largest seismic event at The Geysers with M_W 4.68 occurred in the area where the vertical extent of the seismicity is reaching over 2 km. The estimated maximum magnitude based on geometrical constraints is lower than the one predicted by equation (4), however still significantly larger than the observed maximum magnitude in Prati-9/Prati-29 system. Nevertheless, the geometrical constraint of the reservoir itself seems to provide a conservative first-order approximation of maximum observed magnitude in the analyzed area.

5.2.2. Maximum Magnitude and Size of the Seismicity Cloud

We found a very good correlation ($R = 0.85$) between the long-term temporal changes of average injection rate calculated in a moving time window of 150 days and the cluster volume (Figure 9) approximated with the ellipsoid. Increasing injection rate typically occurs during winter seasons causing the cloud of the seismicity to expand, and to contract at lower injection rates, in agreement with conceptual models presented [*Stark*, 2003; *Beall and Wright*, 2010]. *Shapiro et al.* [2011] suggested that the size of the stimulated volume restricts the occurrence probability of strong events. They proposed the maximum possible magnitude of an earthquake is related to the scale factor Y, which is a function of the length of principal axes of an ellipsoid representing the stimulated volume,

$$M_W^{max,ellipsoid} = 2\log_{10}Y + (\log_{10}\Delta\sigma - \log_{10}C)/1.5 - 6.03, \qquad (6)$$

where $\Delta\sigma$ is the average static stress drop and $C \cong 1$. *Shapiro et al.* [2011] noted an empirical correlation between the observed maximum magnitude and the length of the smallest principal axis of the ellipsoid, L_{min}. Assuming $Y = L_{min}$, an average stress drop of $\Delta\sigma = 7$ MPa and a minimum axis length of $L_{min} = 285$ m, which is the average value for the whole analyzed period of time, maximum magnitude of induced events is predicted to be $M_W^{max,ellipsoid} = 3.4$. This value is close to the observed maximum magnitude of $M_W^{max,obs} = 3.2$ (recalculated from M_D) or $M_W^{max,obs} = 3.4$ (spectral ratio refinement) at the investigated site. Therefore, we speculate that for the Prati-9 and Prati-29 system the maximum magnitude could be

capped by the maximum cluster volume reached. This also corresponds to the average injection rate. Interestingly, we noted that the majority of large events are contained within the stimulated volume (Figure 7).

5.2.3. Low Seismic Efficiency in Hydrothermal Systems and Maximum Magnitude

McGarr [2014] noted that the maximum magnitude predicted with equations (4) and (5) should be considered as "*plausible, but somewhat uncertain, upper bound.*" As the author already pointed out, the actual seismic energy release could be easily smaller, e.g., due to aseismic deformation of stimulated volume or high permeability of the stimulated formation, resulting in little to no pore pressure increase (see also discussion in *Maxwell et al.* [2008]). Indeed, the observed magnitudes in this study are nearly 2 orders of magnitude lower than predicted by equation (4). This can be attributed to The Geysers hydrothermal system being a vapor-dominated reservoir, where the actual net fluid volume and fluid pore pressure are seriously affected by fluid vaporization, rendering the usage of equation (4) problematic. In our case the pore pressure build up is relatively small because (1) the gaseous in situ pore fluid is much more compliant than pore fluids in liquid-filled reservoirs and (2) the injected water displaces vapor which has lower viscosity than liquid water. The latter has a similar effect as high permeability in the context of the Darcy's law:

$$Q = \frac{k}{\eta} A \frac{dP}{dx},\tag{7}$$

where Q is the flow rate, k is the permeability, η is viscosity, A is the cross-section area, and $\frac{dP}{dx}$ is the pressure gradient. As a consequence, the additional energy supplied to the reservoir by fluid injection quickly dissipates due to the high mobility ($= k/\eta$) of fluids resulting in lower pressure increase. The maximum pore pressure change between preinjection/postinjection periods and peak injection period at Prati-9/Prati-29 was estimated to be approx. $\Delta P^{\mathrm{max}} = 1$ MPa [*Martínez-Garzón et al.*, 2014]. Interestingly, one could replace the uncertain $\frac{1}{3}(3\lambda + 2G)\Delta V$ term in right-hand side of equation (4) with $V\overline{\Delta P}$ (cf. equation (1) in *McGarr* [2014]), where V is the volume of formation weakened by injection of fluids and $\overline{\Delta P}$ is the average increase in the pore pressure in the volume V, leading to the following formula for the maximum magnitude:

$$M_0^{\mathrm{max},\Delta P,V} = \frac{1-B}{B} 2\mu V\overline{\Delta P}.\tag{8}$$

Assuming $b = 1.22$, $\mu = 0.68$, $\Delta P = 1$ MPa (note that we assumed $\overline{\Delta P} = \Delta P^{\mathrm{max}}$), and volume of formation weakened by injection of fluids corresponding to the volume of ellipsoid at the time of occurrence of LME ($V \cong 385$ Mm^3; cf. Figure 9), this corresponds to $M_0^{\mathrm{max},\Delta P,V} = 1.2 \times 10^{14}$ or $M_W^{\mathrm{max},\Delta P,V} = 3.32$, being in good agreement with the observed maximum magnitude.

It is worth to note that low seismic efficiency is also observed in other hydrothermal systems and caution must be taken while discussing the maximum magnitude in these type of reservoirs. For example, in the Berlín Geothermal Field, El Salvador [*Ruggeri et al.*, 2006], over 3×105 m^3 of water was injected into a reservoir with temperatures of about 300° during three injection stages at the well TR8A [*Kwiatek et al.*, 2013, 2014]. The fluid injection resulted in a cluster of seismicity with a maximum event magnitude of 1.7 (cf. Figure 5b). Also, at the Newberry EGS system, where the reservoir temperatures exceed 316°C [*Osborn et al.*, 2011] the maximum observed magnitude was 2.4 during injection of over 4×104 m^3 of water [*Cladouhos et al.*, 2013].

6. Conclusions

We investigated a 7 year long fluid injection performed in two wells at the northwestern Geysers geothermal field in California studying properties of the associated seismicity recorded in the vicinity of the injection sites. We also discussed the constraints on the maximum expected magnitude due to injecting over 10.5 Mm^3 of treated wastewater in the two wells of the area. We find the following:

1. Changes in long-term spatial, temporal, and seismic source characteristics are clearly attributed to variations in injection flow rates and that hypocenters tend to migrate toward greater depths of the reservoir with time.
2. The large discrepancy in seismic moment release and seismic activity for Prati-9 and Prati-29 wells may be explained by differences in thermal stresses resulting from different water and/or host rock temperatures at both wells as well as increasing pore pressure and poroelastic effects that tend to dominate at greater depths.

3. Increasing poroelastic stresses at greater depths affect the kinematic properties of the seismicity in that at reservoir depths normal faulting mechanism events dominate, whereas at larger depths the contribution of strike-slip events is significantly increasing.

4. In the Prati-9/Prati-29 two-well system the observed maximum magnitude is in agreement with suggested models that relate the expected maximum magnitude to the dimensions of the seismic cloud. Alternatively, the maximum expected magnitude may be assessed using volume of formation weakened by fluid injection (approximate volume of seismicity cloud) and average pore pressure change.

5. The observed seismic energy release and the seismic efficiency in The Geysers are small compared to the energy from fluid injection.

References

Abercrombie, R. E. (1995), Earthquake source scaling relationships from −1 to 5 ML using seismograms recorded at 2.5-km depth, *J. Geophys. Res.*, *100*, 24,015–24,036, doi:10.1029/95JB02397.

Altmann, J. B., B. I. R. Müller, T. M. Müller, O. Heidbach, M. R. P. Tingay, and A. Weißhardt (2014), Pore pressure stress coupling in 3D and consequences for reservoir stress states and fault reactivation, *Geothermics*, doi:10.1016/j.geothermics.2014.01.004.

Andersen, L. M. (2001), *A Relative Moment Tensor Inversion Technique Applied to Seismicity Induced by Mining*, Univ. of the Witwatersrand, Johannesburg.

Bachmann, C. E., S. Wiemer, B. P. Goertz-Allmann, and J. Woessner (2012), Influence of pore-pressure on the event-size distribution of induced earthquakes, *Geophys. Res. Lett.*, *39*, L09302, doi:10.1029/2012GL051480.

Baisch, S., R. Weidler, R. Vörös, D. Wyborn, and L. de Graaf (2006), Induced Seismicity during the Stimulation of a Geothermal hfr Reservoir in the Cooper Basin, Australia, *Bull. Seismol. Soc. Am.*, *96*(6), 2242–2256.

Beall, J., and M. Wright (2010), Southern extent of The Geysers high temperature reservoir based on seismic and geochemical evidence, *Geotherm. Resour. Counc. Trans.*, *34*, 1199–1202.

Beall, J., M. Wright, A. Pingol, and P. Atkinson (2010), Effect of high rate injection on seismicity in the Geysers, *Geotherm. Resour. Counc. Trans.*, *34*, 1203–1208.

Boatwright, J. (1978), Detailed spectral analysis of two small New York State earthquakes, *Bull. Seismol. Soc. Am.*, *68*, 1131–1177.

Boatwright, J., and D. M. Boore (1982), Analysis of the ground accelerations radiated by the 1980 Livermore Valley earthquakes for directivity and dynamic source characteristics, *Bull. Seismol. Soc. Am.*, *72*(6A), 1843–1865.

Boyle, K., and M. Zoback (2014), The stress state of the Northwest Geysers, California geothermal field, and implications for fault-controlled fluid flow, *Bull. Seismol. Soc. Am.*, *104*(5), 2303–2312.

Cesca, S., F. Grigoli, S. Heimann, Á. González, E. Buforn, S. Maghsoudi, E. Blanch, and T. Dahm (2014), The 2013 September–October seismic sequence offshore Spain: A case of seismicity triggered by gas injection?, *Geophys. J. Int.*, *198*(2), 941–953.

Cladouhos, T., S. Petty, Y. Nordin, M. Moore, K. Grasso, M. Uddenberg, M. Sawyer, B. Julian, and G. R. Foulger (2013), Microseismic monitoring of Newberry volcano EGS demonstration, in *38th Workshop on Geothermal Reservoir Engineering, Stanford Geothermal Program Workshop Rep.*, 38, pp. 778–786, Stanford Univ., Stanford, Calif.

Convertito, V., N. Maercklin, N. Sharma, and A. Zollo (2012), From induced seismicity to direct time-dependent seismic hazard, *Bull. Seismol. Soc. Am.*, *102*(6), 2563–2573.

Convertito, V., A. Zollo, N. Sharma, A. Orefice, and A. Emolo (2015), Earthquake source parameters and scaling relationships at The Geysers geothermal field, California, in *Proceedings of AGIS Workshop on Induced Seismicity, 10-30 March 2015*, Davos Schatzalp, Swiss Seismolog. Serv., Switzerland.

Dahm, T. (1996), Relative moment tensor inversion based on ray theory: Theory and synthetic tests, *Geophys. J. Int.*, *124*, 145–257.

Davi, R., V. Vavryčuk, E.-M. Charalampidou, and G. Kwiatek (2013), Network sensor calibration for retrieving accurate moment tensors of acoustic emissions, *Int. J. Rock Mech. Min. Sci.*, *62*, 59–67, doi:10.1016/j.ijrmms.2013.04.004.

Deichmann, N., and D. Giardini (2009), Earthquakes induced by the stimulation of an enhanced geothermal system below Basel (Switzerland), *Seismol. Res. Lett.*, *80*(5), 784–798, doi:10.1785/gssrl.80.5.784.

Dempsey, D., and J. Suckale (2015), Overview of the northwest Geysers EGS demonstration project, in *Proceedings of the 40th Workshop on Geothermal Reservoir Engineering*, p. SGP–TR–204, Stanford Univ., Stanford, Calif.

Eaton, D. W., J. Davidsen, P. K. Pedersen, and N. Boroumand (2014), Breakdown of the Gutenberg-Richter relation for microearthquakes induced by hydraulic fracturing: Influence of stratabound fractures, *Geophys. Prospect.*, *62*(4), 806–818, doi:10.1111/1365-2478.12128.

Eberhart-Phillips, D., and D. H. Oppenheimer (1984), Induced seismicity in The Geysers geothermal area, California, *J. Geophys. Res.*, *89*(B2), 1191–1207, doi:10.1029/JB089iB02p01191.

Edwards, B., and J. Douglas (2014), Magnitude scaling of induced earthquakes, *Anal. Induced Seism. Geotherm. Oper.*, *52*, 132–139, doi:10.1016/j.geothermics.2013.09.012.

Ellsworth, W. L. (2013), Injection-induced earthquakes, *Science*, *341*(6142), doi:10.1126/science.1225942.

Eshelby, J. D. (1957), The determination of the elastic field of an ellipsoidal inclusion, and related problems, *Proc. R. Soc. London, Ser. A*, *241*(1226), 376–396, doi:10.1098/rspa.1957.0133.

Evans, K. F., A. Zappone, T. Kraft, N. Deichmann, and F. Moia (2012), A survey of the induced seismic responses to fluid injection in geothermal and CO_2 reservoirs in Europe, *Geothermics*, *41*, 30–54, doi:10.1016/j.geothermics.2011.08.002.

Fjær, E., and H. Ruistuen (2002), Impact of the intermediate principal stress on the strength of heterogeneous rock, *J. Geophys. Res.*, *107*(B2), 2032, doi:10.1029/2001JB000277.

Garcia, J., M. Walters, J. Beall, C. Hartline, A. Pingol, S. Pistone, and M. Wright (2012), Overview of the northwest Geysers EGS demonstration project, in *Proceedings of the 37th Workshop on Geothermal Reservoir Engineering*, p.SGP–TR–194, Stanford Univ., Stanford, Calif.

Giardini, D. (2009), Geothermal quake risks must be faced, *Nature*, *462*(7275), 848–849, doi:10.1038/462848a.

Goertz-Allmann, B. P., A. Goertz, and S. Wiemer (2011), Stress drop variations of induced earthquakes at the Basel geothermal site, *Geophys. Res. Lett.*, *38*, L09308, doi:10.1029/2011GL047498.

Goyal, K. P. (1998), Overview of the northwest Geysers EGS demonstration project, in *Proceedings of the 23rd Workshop on Geothermal Reservoir Engineering*, p.SGP–TR–158, Stanford Univ., Stanford, Calif.

Gritto, R., and S. P. Jarpe (2014), Temporal variations of V_P/V_S-ratio at The Geysers geothermal field, USA, *Anal. Induced Seism. Geotherm. Oper.*, *52*, 112–119, doi:10.1016/j.geothermics.2014.01.012.

Hanks, T. C., and H. Kanamori (1979), A moment magnitude scale, *J. Geophys. Res.*, *84*, 2348–2350, doi:10.1029/JB084iB05p02348.

Hardebeck, J. L., and A. J. Michael (2006), Damped regional-scale stress inversions: Methodology and examples for southern California and the Coalinga aftershock sequence, *J. Geophys. Res.*, *111*, B11310, doi:10.1029/2005JB004144.

Hardebeck, J. L., and P. M. Shearer (2002), A new method for determining first-motion focal mechanisms, *Bull. Seismol. Soc. Am.*, *92*, 2264–2276, doi:10.1785/0120010200.

Harrington, R. M., G. Kwiatek, and S. M. Moran (2015), Self-similar rupture implied by scaling properties of volcanic earthquakes occurring during the 2004–2008 eruption of Mount St. Helens, Washington, *J. Geophys. Res. Solid Earth*, *120*, 4966–4982, doi:10.1002/2014JB011744.

Hartzell, S. H. (1978), Earthquake aftershocks as Green's functions, *Geophys. Res. Lett.*, *5*, 1–5, doi:10.1029/GL005i001p00001.

Hastings, W. K. (1970), Monte Carlo sampling methods using Markov chains and their applications, *Biometrica*, *57*(1), 97–109.

Holland, A. A. (2013), Earthquakes triggered by hydraulic fracturing in south-central Oklahoma, *Bull. Seismol. Soc. Am.*, *103*(3), 1784–1792.

Horton, S. (2012), Disposal of hydrofracking waste fluid by injection into subsurface aquifers triggers earthquake swarm in central Arkansas with potential for damaging earthquake, *Seismol. Res. Lett.*, *83*(2), 250–260.

Husen, S., E. Kissling, and A. Deschwanden (2012), Induced seismicity during the construction of the Gotthard Base Tunnel, Switzerland: Hypocenter locations and source dimensions, *J. Seismol.*, *16*(2), 195–213, doi:10.1007/s10950-011-9261-8.

Jeanne, P., J. Rutqvist, C. Hartline, J. Garcia, P. F. Dobson, and M. Walters (2014), Reservoir structure and properties from geomechanical modeling and microseismicity analyses associated with an enhanced geothermal system at The Geysers, California, *Geothermics*, *51*, 460–469, doi:10.1016/j.geothermics.2014.02.003.

Kagan, Y. Y. (1991), 3-D rotation of double-couple earthquake sources, *Geophys. J. Int.*, *106*, 709–716.

Kagan, Y. Y. (2007), Simplified algorithms for calculating double-couple rotation, *Geophys. J. Int.*, *171*(1), 411–418.

Kim, W.-Y. (2013), Induced seismicity associated with fluid injection into a deep well in Youngstown, Ohio, *J. Geophys. Res. Solid Earth*, *118*, 3506–3518, doi:10.1002/jgrb.50247.

Klein, F. (2006), Y2000 Shadow Format and NCSN data codes.

Kwiatek, G. (2008), Relative source time function deconvolution at the Rudna copper mine: Uncertainty Estimation, *J. Seismol.*, *12*(4), 499–517, doi:10.1007/s10950-008-9100-8.

Kwiatek, G., K. Plenkers, and G. Dresen (2011), Source parameters of picoseismicity recorded at Mponeng Deep Gold Mine, South Africa: Implications for scaling relations, *Bull. Seismol. Soc. Am.*, *101*(6), 2592–2608, doi:10.1785/0120110094.

Kwiatek, G., M. Bohnhoff, P. Martínez-Garzón, F. Bulut, and G. Dresen (2013), High-resolution reservoir characterization using induced seismicity and state of the art waveform processing techniques, *First Break*, *31*(7), 81–88.

Kwiatek, G., F. Bulut, M. Bohnhoff, and G. Dresen (2014), High-resolution analysis of seismicity induced at Berlín geothermal field, El Salvador, *Geothermics*, *52*, 98–111, doi:10.1016/j.geothermics.2013.09.008.

Lasocki, S. (2005), Probabilistic analysis of seismic hazard posed by mining induced events, in *Proc. 6th Int. Symp. on Rockburst in Mines, Controling Seismic Risk"*, edited by Y. Potvin and M. Hudyma, pp. 555–560, ACG, Perth, Australia.

Lasocki, S., and B. Orlecka-Sikora (2008), Seismic hazard assessment under complex source size distribution of mining-induced seismicity, *Tectonophysics*, *456*(1–2), 28–37, doi:10.1016/j.tecto.2006.08.013.

Lockner, D. A., R. Summers, D. Moore, and J. D. Byerlee (1982), Laboratory measurements of reservoir rock from the Geysers geothermal field, California, *Int. J. Rock Mech. Min. Sci. Geomech. Abstr.*, *19*(2), 65–80, doi:10.1016/0148-9062(82)91632-1.

Madariaga, R. (1976), Dynamics of an expanding circular fault, *Bull. Seismol. Soc. Am.*, *66*, 639–666.

Majer, E. L., and J. E. Peterson (2007), The impact of injection on seismicity at The Geysers, California Geothermal Field, *Int. J. Rock Mech. Min. Sci.*, *44*(8), 1079–1090, doi:10.1016/j.ijrmms.2007.07.023.

Majer, E. L., R. Baria, M. Stark, S. Oates, J. Bommer, B. Smith, and H. Asanuma (2007), Induced seismicity associated with enhanced geothermal systems, *Geothermics*, *36*(3), 185–222, doi:10.1016/j.geothermics.2007.03.003.

Martínez-Garzón, P., M. Bohnhoff, G. Kwiatek, and G. Dresen (2013), Stress tensor changes related to fluid injection at The Geysers geothermal field, California, *Geophys. Res. Lett.*, *40*, 2596–2601, doi:10.1002/grl.50438.

Martínez-Garzón, P., G. Kwiatek, H. Sone, M. Bohnhoff, G. Dresen, and C. Hartline (2014), Spatiotemporal changes, faulting regimes, and source parameters of induced seismicity: A case study from The Geysers geothermal field, *J. Geophys. Res. Solid Earth*, *119*, 8378–8396, doi:10.1002/2014JB011385.

Martínez-Garzón, P., G. Kwiatek, M. Ickrath, and M. Bohnhoff (2014), MSATSI: A MATLAB package for stress inversion combining solid classic methodology, a new simplified user-handling, and a visualization tool, *Seismol. Res. Lett.*, *85*(4), 896–904, doi:10.1785/0220130189.

Maxwell, S. C., J. E. Shemeta, E. Campbell, and D. J. Quirk (2008), *Microseismic Deformation Rate Monitoring, in SPE-116596-MS*, Society of Petroleum Engineers, SPE.

McGarr, A. (2014), Maximum magnitude earthquakes induced by fluid injection, *J. Geophys. Res. Solid Earth*, *119*, 1008–1019, doi:10.1002/2013JB010597.

Metropolis, N., A. Rosenbluth, M. Rosenbluth, A. Teller, and E. Teller (1953), Equation of state calculations by fast computing machines, *J. Chem. Phys.*, *21*, 1087–1092.

Michael, A. J. (1987), Use of focal mechanisms to determine stress: A control study, *J. Geophys. Res.*, *92*, 357–369, doi:10.1029/JB092iB01p00357.

Mosegaard, K., and A. Tarantola (1995), Monte Carlo sampling of solutions to inverse problems, *J. Geophys. Res.*, *100*(B7), 12,431–12,447, doi:10.1029/94JB03097.

Mueller, C. S. (1985), Source pulse enhancement by deconvolution of an empirical Green's function, *Geophys. Res. Lett.*, *12*(1), 33–36, doi:10.1029/GL012i001p00033.

Osborn, W. L., S. Petty, T. T. Cladouhos, J. Iovenitti, L. Nofziger, O. Callahan, D. S. Perry, and P. L. Stern (2011), *Newberry Volcano EGS Demonstration-Phase I Results*, AltaRock Energy, Inc., Seattle, Wash.

Percival, D. B., and A. T. Walden (1993), *Spectral Analysis for Physical Applications: Multitaper and Conventional Univariate Techniques*, Cambridge Univ. Press, Cambridge, U. K.

Reasenberg, P., and D. Oppenheimer (1985), FPFIT, FPPLOT, and FPPAGE: FORTRAN computer programs for calculating and displaying earthquake fault-plane solutions, *U.S. Geol. Surv. Open-File Rep.*, *85*(739), 109.

Ruggeri, G., C. M. Petrone, G. Gianelli, A. Arias, and E. Torio Enriquez (2006), Hydrothermal alteration in the Berlin geothermal field (El Salvador): new data and discussion on the natural state of the system, *Period. Mineral.*, *75*(2–3), 293–312.

Rutqvist, J., C. M. Oldenburg, (2008), Analysis of injection-induced micro-earthquakes in a geothermal steam reservoir, Geysers Geothermal Field, California, *Proceedings of the 42th U.S. Rock Mechanics Symposium, San Francisco, California, USA, June 29–July 2, 2008*, Am. Rock Mechanics Assoc., Pap., 151.

Rutqvist, J., P. Dobson, J. Garcia, C. Hartline, P. Jeanne, C. Oldenburg, D. Vasco, and M. Walters (2015), The northwest Geysers EGS demonstration project, California: Pre-stimulation modeling and interpretation of the stimulation, *Math. Geosci.*, *47*(1), 3–29, doi:10.1007/s11004-013-9493-y.

Schoenball, M., T. M. Müller, B. I. R. Müller, and O. Heidbach (2010), Fluid-induced microseismicity in pre-stressed rock masses, *Geophys. J. Int.*, *180*(2), 813–819, doi:10.1111/j.1365-246X.2009.04443.x.

Segall, P., and S. D. Fitzgerald (1998), A note on induced stress changes in hydrocarbon and geothermal reservoirs, *Tectonophysics*, *289*(1–3), 117–128, doi:10.1016/S0040-1951(97)00311-9.

Shapiro, S. A., C. Dinske, and J. Kummerow (2007), Probability of a given-magnitude earthquake induced by a fluid injection, *Geophys. Res. Lett.*, *34*, L22314, doi:10.1029/2007GL031615.

Shapiro, S. A., O. S. Krüger, C. Dinske, and C. Langenbruch (2011), Magnitudes of induced earthquakes and geometric scales of fluid-stimulated rock volumes, *Geophysics*, *76*(6), WC55–WC63, doi:10.1190/geo2010-0349.1.

Sharma, N., V. Convertito, N. Maercklin, and A. Zollo (2013), Ground-motion prediction equations for The Geysers geothermal area based on induced seismicity records, *Bull. Seismol. Soc. Am.*, *103*(1), 117–130, doi:10.1785/0120120138.

Shearer, P. M., G. Prieto, and E. Hauksson (2006), Comprehensive analysis of earthquake source spectra in southern California, *J. Geophys. Res.*, *111*, B06303, doi:10.1029/2005JB003979.

Stark, M. (1992), Microearthquakes - A tool to track injected water in The Geysers reservoir, in *Monograph on The Geysers Geothermal Field, Geothermal Resources Council Special Report*, vol. 17, edited by C. Stone, pp. 111–117, Geothermal Resour. Council, Davis, Calif.

Stark, M. (2003), Seismic evidence for a long-lived enhanced geothermal system (EGS) in the Northern Geysers Reservoir, *Trans.-Geotherm. Resour. Counc.*, 727–732.

Takahashi, M., and H. Koide (1989), *Effect of Intermediate Principal Stress on Strength and Deformation Behavior of Sedimentary Rocks at the Depth Shallower than 2000 m*, pp. 19–26, Balkema, Brookfield.

Viegas, G., and L. Hutchings (2011), Characterization of induced seismicity near an injection well at the northwest Geysers geothermal field, California, *Geotherm. Resour. Counc. Trans.*, *35*, 1773–1780.

Waldhauser, F., and W. L. Ellsworth (2000), A double-difference earthquake location algorithm: Method and application to the Northern Hayward Fault, California, *Bull. Seismol. Soc. Am.*, *90*(6), 1353–1368, doi:10.1785/0120000006.

Wiemer, S., and M. Wyss (2000), Minimum magnitude of completeness in earthquake catalogs: Examples from Alaska, the Western United States & Japan, *Bull. Seismol. Soc. Am.*, *90*, 859–869.

Zang, A., V. Oye, P. Jousset, N. Deichmann, R. Gritto, A. McGarr, E. Majer, and D. Bruhn (2014), Analysis of induced seismicity in geothermal reservoirs – An overview, *Anal. Induc. Seism. Geotherm. Oper.*, *52*, 6–21, doi:10.1016/j.geothermics.2014.06.005.

Zollo, A., A. Orefice, and V. Convertito (2014), Source parameter scaling and radiation efficiency of microearthquakes along the Irpinia fault zone in southern Apennines, Italy, *J. Geophys. Res. Solid Earth*, *119*, 3256–3275, doi:10.1002/2013JB010116.